Energy Storage Materials 47 (2022) 113–121

Contents lists available at ScienceDirect

Energy Storage Materials

journal homepage: www.elsevier.com/locate/ensm

Tuning electrolyte solvation structures to enable stable aqueous Al/MnO_2 battery

Yan Xu[a,d], Jiale Ma[c], Taoli Jiang[a], Honghe Ding[b], Weiping Wang[a], Mingming Wang[a], Xinhua Zheng[a], Jifei Sun[a,d], Yuan Yuan[a], Mingyan Chuai[a], Na Chen[a], Zhenyu Li[c,*], Hanlin Hu[d,*], Wei Chen[a,*]

[a] Department of Applied Chemistry, School of Chemistry and Materials Science, Hefei National Laboratory for Physical Sciences at the Microscale, University of Science and Technology of China, Hefei, Anhui 230026, China
[b] National Synchrotron Radiation Laboratory, University of Science and Technology of China, Hefei, Anhui 230026, China
[c] Hefei National Laboratory for Physical Sciences at the Microscale, University of Science and Technology of China, Hefei, Anhui 230026, China
[d] Hoffman Institute of Advanced Materials, Shenzhen Polytechnic, Shenzhen, Guangdong 518000, China

ARTICLE INFO

Keywords:
Electrolyte solvation structure
MnO_2 cathode
MnO_2/Mn^{2+} chemistry
Long cycle life
Al/MnO_2 battery

ABSTRACT

MnO_2 is regarded as a promising cathode material owing to its low cost, environmental friendliness and high theoretical capacity. However, it is plagued by sluggish intercalation/extraction of multivalent cations into MnO_2 lattice structure in diluted electrolytes, leading to short cycle life and fast capacity decay of aqueous MnO_2 cathode. Here, we select Al/MnO_2 aqueous battery as a demonstration and report a new approach of using concentrated aqueous electrolytes to tune the solvation structures of Al^{3+} cations to eliminate their intercalation into MnO_2, ensuring high reversibility of MnO_2 cathode in the MnO_2/Mn^{2+} deposition/stripping chemistry. Molecular dynamics simulation and experimental analysis reveal that the radius of Al^{3+} solvation sheath in the concentrated aqueous electrolytes is larger than the lattice spacing of MnO_2, thereby avoiding their intercalation into the MnO_2 cathode. As a result, the newly developed Al/MnO_2 full cell in the optimized electrolyte delivers a high discharge voltage of ~1.9 V, large specific capacity of ~493 mAh/g and long-term stability of over 1000 cycles. This work provides new opportunities to the development of highly reversible MnO_2 cathode for aqueous multivalent metal/MnO_2 batteries.

1. Introduction

Rechargeable Al batteries emerge as competitive alternatives to lithium batteries [1–4], because Al possesses high volumetric (8046 mAh/cm^3) and gravimetric (2980 mAh/g) energy densities, as well as a low redox potential of Al^{3+}/Al (−1.67 V *vs.* SHE) [5,6]. Moreover, the high abundance, low-cost and easy accessibility of Al resources enable Al batteries promising candidates for different energy storage systems [7]. However, the lack of suitable cathode materials has been a critical issue that prohibits the application of Al batteries. Recently, two categories of cathode materials have been developed for rechargeable Al batteries. One is carbon-based materials with high specific surface areas such as 3D graphite-foam [8] and defect-free graphene [9] that can accommodate intercalation of $Al_xCl_y^-$ anions, delivering high power density of 30 kW/kg due to the fast monovalent reaction kinetics. However, the output specific capacity was largely restrained by the monovalent charge storage characteristics. The other category of cathode materials is based on Al^{3+} cations intercalation/extraction mechanism, which can realize high specific capacities. However, the discharge rate is usually low in these cathode materials because of the sluggish transport kinetics of Al^{3+} in the lattice structures [10–12]. For example, in the reported V_2O_5 [13], CuHCF [14], spinel MnO_2 materials [15], Al^{3+} cations always have sluggish intercalation/extraction kinetics, leading to short cycling life (usually less than 100 cycles), fast capacity decay with relatively low discharge plateau (typically ranging from 0.3 V to 0.8 V *vs.* Al/Al^{3+}), which is hardly considered as practical cathode materials for the Al batteries. Particularly, MnO_2 materials are promising cathodes for Al batteries owing to their earth abundance, low-cost, environmental friendliness and high theoretical capacity. [16–19] Recent progress on Mn-based cathode materials including α-MnO_2 [16], Birnessite MnO_2 [17], $Al_xMnO_2{\cdot}nH_2O$ [15, 20], α-MnO_2@Mn_2AlO_4 [21] revealed that MnO_2 can be excellent candidates for aqueous multivalent metal batteries. Although much effort has been devoted to fabricate different types of MnO_2, their charge storage performance based on the Al^{3+} intercalation/extraction mechanism showed poor reversibility, short cycling life and low discharge plateau [16,17]. Therefore, it is highly desirable

* Corresponding authors.
E-mail address: weichen1@ustc.edu.cn (W. Chen).

https://doi.org/10.1016/j.ensm.2022.01.060
Received 28 September 2021; Received in revised form 23 January 2022; Accepted 31 January 2022
Available online 1 February 2022

to develop novel MnO_2 cathode materials or apply new chemistries to tackle the critical issues remained in the intercalation of Al^{3+} into MnO_2 materials.

Recently, Chen et al. developed a new MnO_2 cathode in MnO_2/Mn^{2+} deposition/dissolution reactions and showed high discharge voltage (~1.23 V *vs.* SHE), large capacity (~616 mAh/g) and ultralong cycle life (over 10,000 cycles), which fundamentally solved the problems of low capacity and poor reversibility of the traditional MnO_2 cathodes [22]. Afterwards, different MnO_2 based battery chemistries, for instance, MnO_2/Zn [23,24], MnO_2_/Cu [25], and MnO_2/Pb [26] have then been reported and demonstrated good electrochemical performance. However, combination of the MnO_2 cathode based on the Mn^{2+}/MnO_2 chemistry with Al anode has never been reported. We anticipate that high capacity and great reversibility of aqueous Al/MnO_2 battery could be achieved by coupling such a MnO_2 cathode with Al anode. Nevertheless, the electrodeposited MnO_2 on the cathode during the charge process have good lattice structures, which may induce Al^{3+} intercalation into their lattice structures during the battery discharge process. The strong electrostatic attraction between Al^{3+} and O atom in MnO_2 will result in the formation of inactive Al_xMnO_2, and eventually lead to the decay of battery performance. Therefore, how to avoid Al^{3+} intercalation into MnO_2 cathode is the key towards the fabrication of a high performance Al/MnO_2 battery in the Mn^{2+}/MnO_2 chemistry. Designing a larger solvation structure of Al^{3+} cations than the MnO_2 lattice to hinder their intercalation is an effective solution, which can be achieved by tuning the electrolyte solvation structures. It was well-recognized that in the concentrated electrolyte, anions and coordination solvents are strongly coordinated with metal ions rather than staying as free ones [31,32], which can form large solvation structures of metal cations in the electrolyte. Therefore, tuning the solvation structure of Al^{3+} in the aqueous Al/MnO_2 battery became a promising strategy to explore.

In this study, we proposed and demonstrated an aqueous Al/MnO_2 battery based on the MnO_2/Mn^{2+} chemistry with high stability by tuning the solvation structure of Al^{3+} through the strategy of concentrating electrolytes for the sake of avoiding Al^{3+} intercalation. In the optimized saturated electrolyte (s-Al/Mn electrolyte composed of 4.4 M $AlCl_3$ and 1 M $MnCl_2$ in H_2O), the solvation structure of Al^{3+} cations are larger than the ones in the diluted electrolyte (d-Al/Mn electrolyte composed of 1 M $AlCl_3$ and 1 M $MnCl_2$ in H_2O). Therefore, self-intercalation of Al^{3+} into MnO_2 lattice can be prohibited thanks to the larger solvation structure of cations in the s-Al/Mn electrolyte, which guarantees the high reversibility of the MnO_2 cathode. Benefiting from the designed electrolyte, the Al/MnO_2 battery shows a high discharge plateau at ~1.9 V and delivers a large capacity of ~ 493 mAh/g with a stable cycle life of over 1000 cycles. This electrolyte tuning strategy can be applied in more multivalent metal/MnO_2 battery systems to avoid the irreversible multivalent metal cations intercalation.

2. Results and discussion

2.1. The solvation structures of Al^{3+} in different electrolytes

In order to investigate the solvation structures of Al^{3+} in the electrolytes of s-Al/Mn and d-Al/Mn, classical molecular dynamics (cMD) were performed. As shown in Fig. 1a and b, s-Al/Mn electrolyte and d-Al/Mn electrolyte were simulated by considering two cuboid areas in dimensions of $7.7 \times 7.7 \times 7.7$ nm^3 and $7.2 \times 7.2 \times 7.2$ nm^3, respectively. Al, Mn, Cl and water molecules were colored by red, orange, blue and white, respectively. Simple point charge/electronic charge (SPC/EC) model was used to describe the water molecules and interatomic potentials of different ions [29]. As shown in Fig. 1c, in the optimized s-Al/Mn electrolyte, one Al^{3+} was bridged with 1.8 Cl^- and 4.2 H_2O to form the solvation structure of $AlCl_{1.8}(H_2O)_{4.2}{}^{1.2+}$. A higher fraction of water was found in the Al^{3+} first coordination sheath in the d-Al/Mn electrolyte, forming $AlCl_{0.9}(H_2O)_{5.1}{}^{2.1+}$ cluster (Fig. 1c). According to the reported literature in other diluted and concentrated electrolytes [30], $AlCl_{0.9}(H_2O)_{5.1}{}^{2.1+}$ should be easy to dissociate to form Al^{3+}, 0.9 Cl^- and 5.1 H_2O in the diluted electrolyte, while high energy barrier was needed to dissociate $AlCl_{1.8}(H_2O)_{4.2}{}^{1.2+}$ in the concentrated electrolyte. The above hypothesis was further verified by calculating the binding energies of solvation clusters of $AlCl_{0.9}(H_2O)_{5.1}{}^{2.1+}$ and $AlCl_{1.8}(H_2O)_{4.2}{}^{1.2+}$ using DFT. As shown in the Figure S1, the binding energy of $AlCl_{0.9}(H_2O)_{5.1}{}^{2.1+}$ is −6.01 eV, while the binding energy of $AlCl_{1.8}(H_2O)_{4.2}{}^{1.2+}$ is −10.01 eV. The higher binding energy of $AlCl_{0.9}(H_2O)_{5.1}{}^{2.1+}$ indicated that it is easier to dissociate to form Al^{3+} ions. The bond distances of Al-O and Al-Cl were calculated to be 2.0 Å and 2.5 Å, respectively (Fig. 1d), and the maximum layer distance of MnO_2 is 1.3 Å. Therefore, $AlCl_{1.8}(H_2O)_{4.2}{}^{1.2+}$ cations are too large to intercalate into the MnO_2 lattice, while the dissociated Al^{3+} cations (0.5 Å) have the chance to intercalate into the MnO_2 lattice.

The hypothetical electro-dissolution processes of MnO_2 in the electrolytes of s-Al/Mn and d-Al/Mn are schematically illustrated in Fig. 1e. In the d-Al/Mn electrolyte, the reduction of MnO_2 in the initial state is related to the dissolution of MnO_2 due to its higher redox potential. In the following stage, some of dissociated Al^{3+} cations (0.5 Å) intercalate into the lattice of MnO_2 (1.3 Å). The intercalated Al^{3+} cations have strong electrostatic attraction with O atom in MnO_2, resulting in the formation of O vacancy. In this case, the intercalated Al^{3+} cations are hard to escape from the lattice structure of MnO_2 due to the sluggish extraction kinetics of Al^{3+} from MnO_2, which lead to the accumulation of inactive Al_xMnO_2. In the s-Al/Mn electrolyte, the cations and anions are hard to dissociate due to the high binding energy, thus, the radius of $AlCl_{1.8}(H_2O)_{4.2}{}^{1.2+}$ cations are large enough to avoid their intercalation into the MnO_2 lattice. Under such circumstance, the electrodeposited MnO_2 is directly reduced to Mn^{2+} in the electrolyte of s-Al/Mn, achieving highly reversible MnO_2/Mn^{2+} reactions. In order to gain deep understanding of the properties of d-Al/Mn and s-Al/Mn electrolytes, ionic conductivity, pH value and viscosity of both electrolytes have been tested. The ionic conductivity was calculated by the impedance spectra in Al||Al symmetric cells at ambient temperature (Figure S2). It revealed that the ionic conductivities decreased from 157 mS/cm to 44 mS/cm when the electrolyte shifted from d-Al/Mn to s-Al/Mn, which was comparable to that of WISE electrolytes [27]. The pH values of d-Al/Mn and s-Al/Mn electrolytes are 0.33 and 4.45, respectively, which are tested by pH meter. The lower pH value is favorable for the dissolution of MnO_2, while it is not the case in our battery systems (Fig. 2), indicating that the solvation structure of Al^{3+} cations is more crucial to the dissolution of MnO_2. The viscosity of d-Al/Mn and s-Al/Mn electrolytes tested by viscometer were 1.66 and 35.90 mPa •s, respectively.

2.2. The electrochemical performance of Al/MnO_2 battery

In order to ensure the deposition/dissolution of MnO_2 within the stability window of d-Al/Mn and s-Al/Mn electrolytes, linear sweep voltammetry (LSV) was conducted to test the electrochemical oxidation stability window using an Al-Pt cell. As shown in Figure S3, the oxidation stability windows of d-Al/Mn and s-Al/Mn electrolytes were 3.0 V and 2.5 V, respectively. Therefore, the charge voltage should be controlled to less than 2.5 V. It is worth to mention that the current peaks in the range of 2.0 V to 2.5 V were not due to the oxygen evolution reaction but the deposition of MnO_2. In order to figure out how the solvation structures of cations affect the dissolution process of MnO_2, we conducted both three-electrode and two-electrode cell measurements in the s-Al/Mn and d-Al/Mn electrolytes. Firstly, the three-electrode cell was setup by using carbon felt as working electrode, Ag/AgCl as reference electrode and Al as counter electrode, which was cycled in the electrolytes of s-Al/Mn and d-Al/Mn under a current density of 2 mA/cm^2. As shown in Fig. 2a, two discharge plateaus can be observed in the d-Al/Mn electrolyte, which were positioned at 1.03 V (*vs.* Ag/AgCl) and 0.77 V (*vs.* Ag/AgCl). According to the reported literature [17], they can be ascribed to the reduction of MnO_2 to Mn^{2+} ($MnO_2 + 4H^+ + 2e^- = Mn^{2+} + 2H_2O$) and the intercalation of Al^{3+} ions

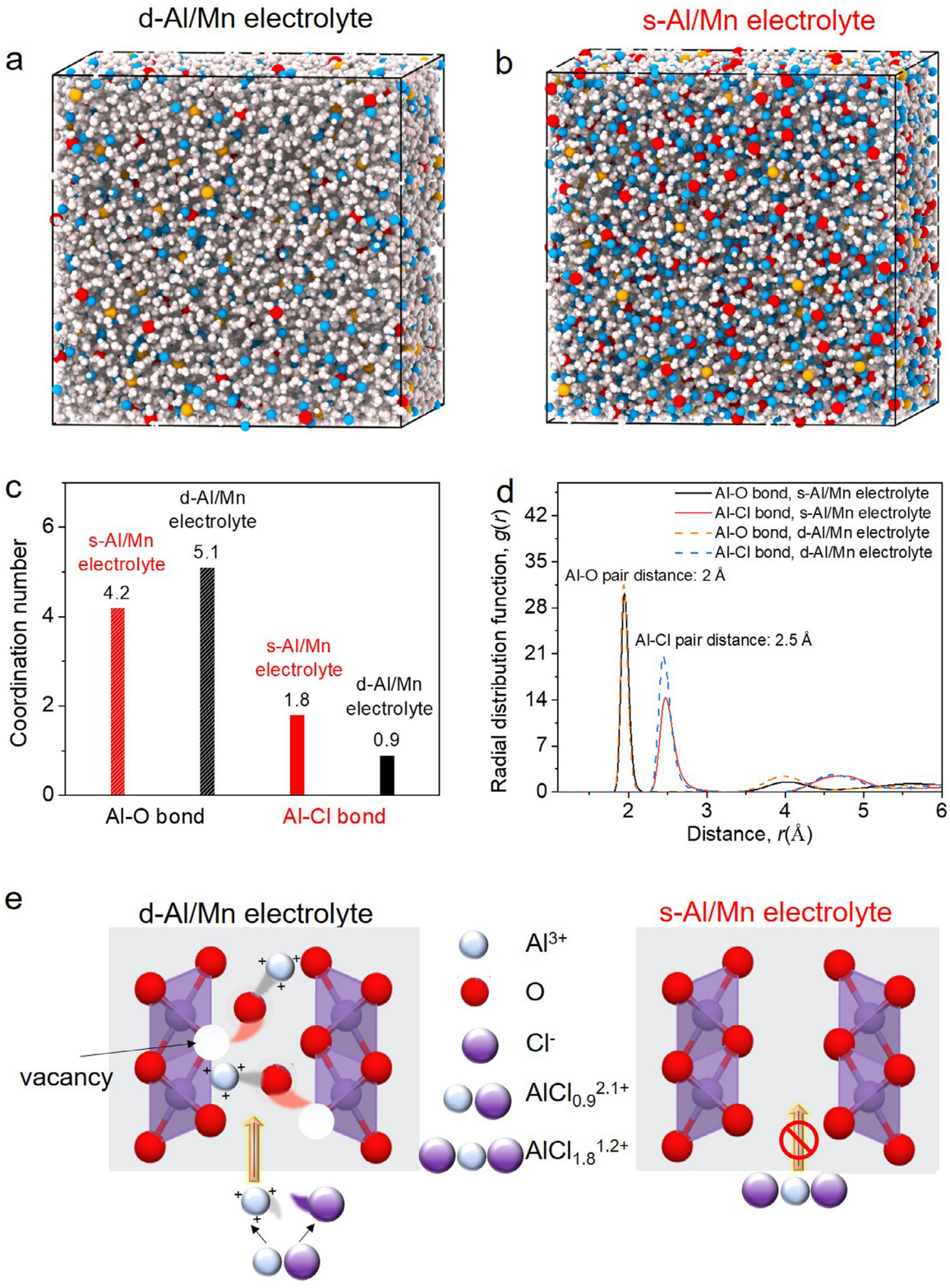

Fig. 1. (a) *c*MD simulated electrolyte structure in the d-Al/Mn electrolyte, where 11190 H_2O (white), 1030 Cl^- (blue), 206 Al^{3+} (red) and 206 Mn^{2+} (orange) molecules were dissolved into a periodic cuboid with dimension of 72.1 × 72.1 × 72.1 Å^3. (b) *c*MD simulated electrolyte structure of the s-Al/Mn electrolyte, where 11,190 H_2O (white), 3130 Cl^- (blue), 906 Al^{3+} (red) and 206 Mn^{2+} (orange) molecules were dissolved into a periodic cuboid with dimension of 77.6 × 77.6 × 77.6 Å^3. (c) The coordination number of Al^{3+} with Cl^- and H_2O in the electrolytes of d-Al/Mn and s-Al/Mn. (d) Radial distribution function of Al-O and Al-Cl pairs. (e) Schematic illustration of electrochemical dissolution process of MnO_2 in the electrolytes of d-Al/Mn and s-Al/Mn.

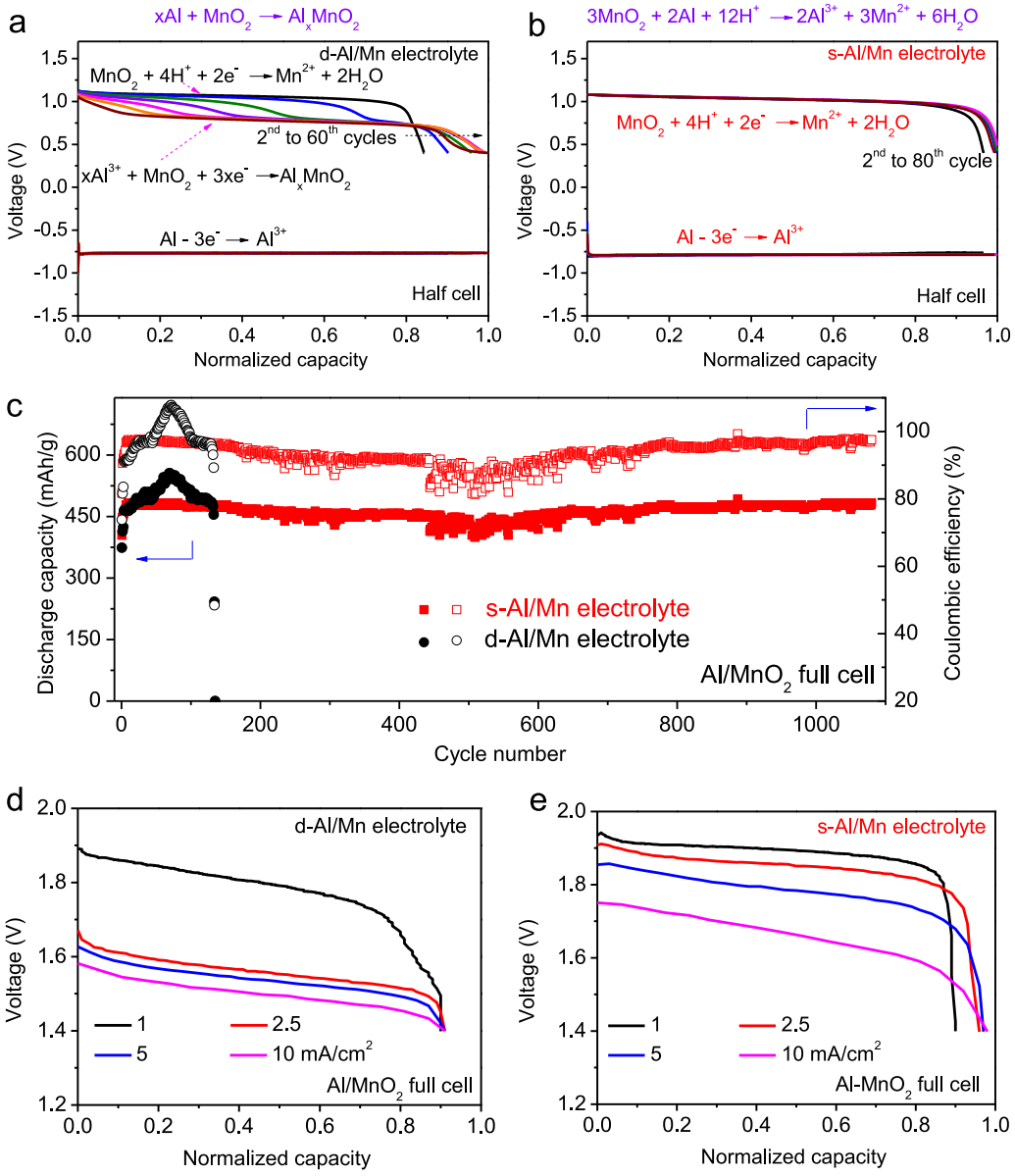

Fig. 2. The voltage profiles of carbon felt (WE)-Ag/AgCl (RE)-Al (CE) three-electrode cell in the electrolytes of (a) d-Al/Mn and (b) s-Al/Mn at the current density of 2 mA/cm^2. (c) The cycling performance of Al/MnO_2 full cell in the electrolytes of s-Al/Mn and d-Al/Mn. The voltage profiles of Al/MnO_2 full cell in the electrolytes of (d) d-Al/Mn and (e) s-Al/Mn with different rates.

into MnO_2 ($xAl^{3+} + MnO_2 + 3xe^- = Al_xMnO_2$). As for the voltage profile of the three-electrode cell in the s-Al/Mn electrolyte, only one distinct discharge plateau positioned at 1.00 V (*vs.* Ag/AgCl) was observed in Fig. 2b, indicating that the reaction was dominated by the reduction of MnO_2 to Mn^{2+} but not the Al^{3+} cations intercalation into MnO_2 during the cell discharge process. It was noticed that an activation process was needed at the first cycle for carbon felt (Figure S4). The core-level spectra of Mn 3 s was utilized to determine the valence states of the deposited MnO_x at different cycles. The average valence numbers of the electrodeposited MnO_2 were calculated to be 3.64 and 3.60 in the electrolytes of d-Al/Mn and s-Al/Mn on the basis of the Mn 3 s peak splitting energy of 4.7 eV and 4.73 eV, respectively (Figure S5). Therefore, the actual electron charge transfer numbers in the Al/MnO_2 cell are 1.64 in the d-Al/Mn electrolyte and 1.60 in the s-Al/Mn electrolyte, respectively. It was revealed that the electrodeposited MnO_2 showed almost the same average oxidation state at the initial cycles. In other words, negligible Al^{3+} ions were intercalated into MnO_2 lattice at initial cycles in both electrolytes. However, at the 80th cycle, the average oxidation state of the MnO_2 cathode dropped to 3.23 in the electrolyte of d-Al/Mn, in contrast, the average oxidation state of the MnO_2 cathode maintained at 3.53 in the electrolyte of s-Al/Mn. Such a change in the electrolyte of d-Al/Mn reflected that Al^{3+} ions were gradually accumulated in the MnO_2 lattice due to the smaller radius of Al^{3+} ions (0.5 Å) compared with MnO_2 lattice (1.3 Å), and the strong electrostatic attraction of Al^{3+} ions with O atom in the MnO_2 host leads to more O vacancy formation. The radius of $AlCl_{1.8}(H_2O)_{4.2}^{1.2+}$ ions are large enough to avoid their intercalation, which evident the importance of tuning the solvation structures of Al^{3+} ions for the reversibility of MnO_2/Mn^{2+} chemistry.

Furthermore, we fabricated two-electrode full cells by using carbon felt as the cathode current collector and Al foil as the anode in both the d-Al/Mn and s-Al/Mn electrolytes, in order to evaluate the influence of the solvation structures of cations in the battery performance. As shown in Fig. 2c, the Al/MnO_2 full cell delivered a stable cycling life over 1000 cycles with a high specific capacity of ~493 mAh/g and Coulombic effi-

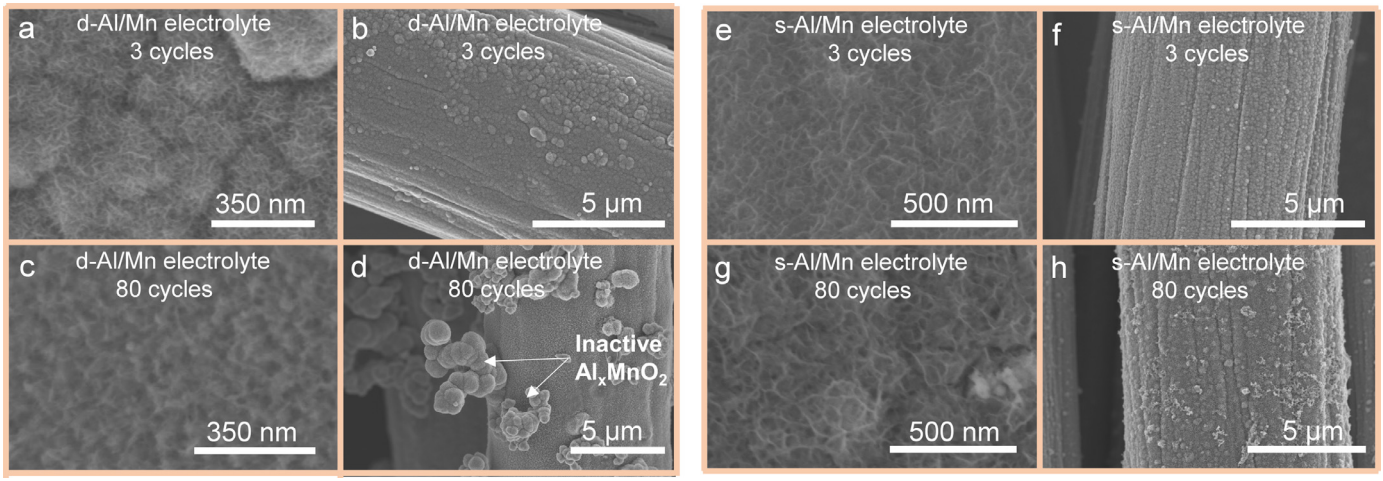

Fig. 3. SEM images of MnO_2 cathodes after (a-b) 3 cycles and (c-d) 80 cycles at charged states in the electrolyte of d-Al/Mn. SEM images of MnO_2 cathodes after (e-f) 3 cycles and (g-h) 80 cycles at charged states in the electrolyte of s-Al/Mn.

ciency of ~97% in the s-Al/Mn electrolyte. Although the Al/MnO_2 full cell delivered a much higher initial discharge capacity (~540 mAh/g), it decayed to 0 mAh/g within 130 cycles in the d-Al/Mn electrolyte. A 7.7-fold improvement in cycle life illustrated that the non-intercalation of Al^{3+} ions was beneficial to the high reversibility of the MnO_2/Mn^{2+} chemistry and the intercalation of Al^{3+} cations was detrimental to the stability of aqueous Al/MnO_2 battery. Al||Al symmetric cells were assembly to verify the reversibility of Al anode at a current density of 1 mA/cm^2. As shown in Figure S6, the Al||Al symmetric cells displayed polarization voltage as high as 0.15 V due to the aluminum oxide passivation layer in both electrolytes. After activation, the polarization voltage dropped to 0.012 V and stably cycled for 140 cycles, indicating the similar behavior of Al anode in both electrolytes. In order to figure out whether H^+ is intercalated into MnO_2, the deposited MnO_2@CF was coupled with Al foil and tested in 0.1 M HCl solution. As presented in Figure S7, no discharge capacity can be detected even in the low cut-off voltage of 1 V (*vs.* Al/Al^{3+}). Previous studies reported that the proton co-intercalation is usually determined by the crystal structure of the electrodes and pH of the electrolyte [28]. In our Al/MnO_2 cells, no evidence was illustrated on the H^+ co-intercalation into the MnO_2. The advantages of the Al/MnO_2 cell using s-Al/Mn electrolyte were further evidenced by the rate capability. At a low discharge rate of 1 mA/cm^2, the voltage plateaus relating to the dissolution of MnO_2 displayed comparable values in the d-Al/Mn and s-Al/Mn electrolytes, which were located at 1.84 V and 1.91 V, respectively. With the discharge rate increased from 1 mA/cm^2 to 10 mA/cm^2, the discharge plateau decreased from 1.84 V to 1.54 V in the electrolyte of d-Al/Mn due to the gradual Al^{3+} ions intercalation into the MnO_2 lattice that causes the sluggish kinetics. In contrast, the discharge plateau of the Al/MnO_2 cell in the s-Al/Mn electrolyte could be well maintained at 1.75 V even at the current density of 10 mA/cm^2. The above electrochemical data showed that tuning the solvation structures of cations provided an effective approach to the prevention of Al^{3+} cations intercalating into MnO_2 lattice and thus the achievement of high-performance Al/MnO_2 batteries.

2.3. Characterizations of MnO_2 cathodes

To gain a deeper insight into the mechanism underlying the encouraging phenomena, scanning electron microscopy (SEM) was carried out to study MnO_2 morphologies after 3 and 80 cycles at the charged states in the electrolytes of d-Al/Mn and s-Al/Mn. As shown in Fig. 3a, the typical nanosheet structure of the deposited MnO_2 could be observed at the 3rd cycle in the electrolyte of d-Al/Mn and the carbon felt was covered with a uniform layer of deposited MnO_2 (Fig. 3b). While the nanosheet structure of the deposited MnO_2 became blurry at the 80th cycle (Fig. 3c) due to the gradually changed MnO_2/Mn^{2+} conversion with cycling life increasing, which can be reflected by a short cycle life (~130 cycles) and unstable discharge plateau in Fig. 2a and 2c. In addition, large aggregations could be observed after 80 cycles (Fig. 3d), which can be ascribed to inactive Al_xMnO_2 accumulation owing to the sluggish extraction kinetics of Al^{3+} out of Al_xMnO_2. With regard to the electrolyte of s-Al/Mn, the nanosheet structure of deposited MnO_2 maintained well at the 80th cycle (Fig. 3g), as compared to that at the 3rd cycle (Fig. 3e). Notably, no large aggregations can be observed even after 80 cycles (Fig. 3f and 3h), implying the good reversibility of the MnO_2 cathode in the MnO_2/Mn^{2+} chemistry by the strategy on tuning the solvation structures of cations. PEIS was further applied to study the MnO_2 cathode of the Al/MnO_2 battery in the electrolytes of d-Al/Mn and s-Al/Mn at different cycles. In order to exclude the effect of Al anode, a three-electrode CF (WE) – Ag/AgCl (RE) – Al (CE) cell was setup by using carbon felt as working electrode, Ag/AgCl as reference electrode and Al as counter electrode. As shown in Figure S8, the interfacial impedance of CF electrode in the electrolyte of d-Al/Mn was significantly increased from the 3rd cycle to the 80th cycle, demonstrating that the undissolved MnO_2 on the CF electrode was gradually accumulated. While the interfacial impedance of CF electrode in the electrolyte of s-Al/Mn at the 3rd cycle was relatively stable as compared to that at the 80th cycle. In addition, the inclined straight line in low frequency region is a crucial indicator to evaluate the diffusion rate of ions to the electrode. As shown in Figure S8a, the diffusion rate of ions in the electrolyte of d-Al/Mn at the 80th cycle decreased dramatically as compared to that at the 3rd cycle. In contrast, the diffusion rate of ions in the electrolyte of s-Al/Mn kept in slight changes with cycling (Figure S8b), implying the high reversibility of the cathode MnO_2 deposition and dissolution. The results of the PEIS measurements further support the morphology changes and electrochemical performances of the Al/MnO_2 battery in the d-Al/Mn and s-Al/Mn electrolytes.

Further, XRD was conducted to check the crystal structures of the deposited MnO_2 after 3, 30 and 80 cycles using d-Al/Mn and s-Al/Mn electrolytes. As shown in Fig. 4a, two peaks positioned at 36.1° and 65.5° belonging to MnO_2 (400) and MnO_2 (002) planes could be observed from the MnO_2 cathode in the electrolyte of d-Al/Mn. With cycling life increased from 3 cycles to 80 cycles, these two MnO_2 peaks shifted to 37.0° and 66.1° gradually, which illustrated the shrinkage of lattice space due to the electrostatic attraction of intercalated Al^{3+} cations to O atoms in MnO_2. While in the electrolyte of s-Al/Mn, no distinct XRD peaks belonging to the electrodeposited MnO_2 could be observed, which may due to the amorphous characteristics or the small particle size of

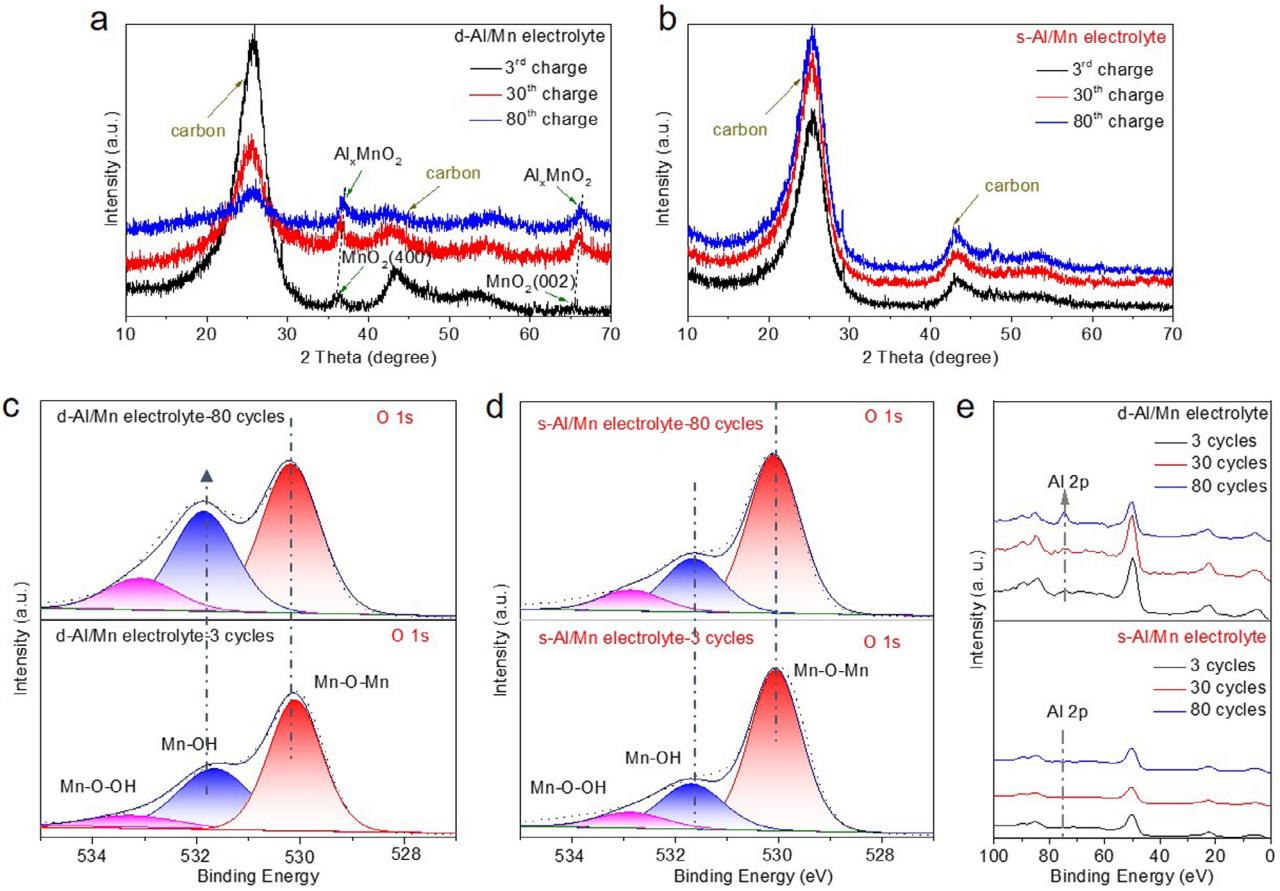

Fig. 4. XRD characterization of the deposited MnO_2 at the charge states after 3, 30 and 80 cycles in (a) d-Al/Mn and (b) s-Al/Mn electrolytes. O 1 s XPS spectra of the deposited MnO_2 at the charge states after 3 and 80 cycles in (c) d-Al/Mn and (d) s-Al/Mn electrolytes. (e) XPS survey spectra of the deposited MnO_2 at the charge states after 3, 30 and 80 cycles in the d-Al/Mn and s-Al/Mn electrolytes.

the electrodeposited MnO_2. The structures of the deposited MnO_2 in different electrolytes were further characterized by transmission electron microscopy (TEM). High-resolution TEM of deposited MnO_2 in the electrolyte of d-Al/Mn showed particle sizes of ~8 nm, and the lattice fringes of 0.24 nm and 0.14 nm correspond to the (002) and (400) planes of MnO_2, respectively (Figure S9). However, the deposited MnO_2 in the electrolyte of s-Al/Mn showed rather amorphous nature with few particles in sizes of only ~2 nm, which may result in the undetectable XRD peaks of the electrodeposited MnO_2. It was noted that the XRD intensity of carbon substrate in the electrolyte of d-Al/Mn became much weaker with the cycling life increased, which indicated the growing accumulation of inactive Al_xMnO_2 on the carbon substance. In contrast, the carbon signals kept in the same intensity with cycling in the electrolyte of s-Al/Mn due to the non-accumulation of inactive Al_xMnO_2 on the carbon substance. These results are in excellent agreements with the SEM observations (Fig. 3). The peak around 29.1° can be ascribed to the XRD holder, because it can be detected from the plain carbon felt on the XRD holder (Figure S10).

X-ray photon spectroscopy (XPS) and X-ray absorption spectroscopy (XAS) tools were further applied to analyze the deposited MnO_2 in the electrolyte of s-Al/Mn. The O 1 s XPS spectra can be split into three components that are associated with the Mn–O–Mn bond (529.7 eV) for tetravalent MnO_2, the Mn–OH bond (531.2 eV) for trivalent MnOOH and the H–O–H bond (532.6 eV) for residual water (Fig. 4c), respectively. With the cycling number increased, the peak intensity of trivalent MnOOH increased greatly in the electrolyte of d-Al/Mn, and this phenomenon further confirmed that Al^{3+} ions intercalate into MnO_2 lattice and attract to O atoms in the host material, resulting in the accumulation of trivalent MnOOH. Binding energy peaks of the Mn 2p XPS spectra exhibited the upward shifts in the electrolyte of d-Al/Mn (Figure S11a). These shifts together with O observation verified the generation of O vacancy in the MnO_2, which was identical to the XRD results. Trivalent MnOOH was detectable in the s-Al/Mn electrolyte because of the imperfection of deposited MnO_2, different from in the d-Al/Mn electrolyte, the peak intensity of trivalent MnOOH kept unchanged even after 80 cycles in O 1 s spectra of the MnO_2 in the s-Al/Mn electrolyte (Fig. 4d), suggesting no $AlCl_{1.8}(H_2O)_{4.2}{}^{1.2+}$ ions intercalated into MnO_2 to induce the generation of O vacancy. As for the XPS survey, the Al 2p peak at 73 eV was growing in the deposited MnO_2 cathodes with cycling in the electrolyte of d-Al/Mn, further verifying the intercalation of Al^{3+} cations into MnO_2 (Fig. 4e). While in the electrolyte of s-Al/Mn, no Al 2p signal can be detected even after 80 cycles (Fig. 4e), which implied that no Al^{3+} cations intercalate into MnO_2 lattice. The highly improved reversibility of the MnO_2/Mn^{2+} chemistry was strongly associated with the solvation structure of Al^{3+}.

The deposited MnO_2 after 3, 30 and 80 cycles were examined by O K-edge X-ray absorption spectroscopy (XAS) to gain insight into their electronic structure change. As presented in Fig. 5a and b, t_{2g} and e_g arise from the hybridization of O 2p with Mn 3d t_{2g} and 3d e_g orbitals, respectively, and the broad peak G is associated with the hybrid states of O 2p with metallic Mn 4sp characters. Therefore, the decrease of the t_{2g} peak indicates the formation of the oxygen vacancy and e_g peak indicates lattice oxygen. As shown in Fig. 5a and c, the relative intensity of t_{2g}/e_g in the O K-edge XAS spectra showed a dramatic decrease in the electrolyte of d-Al/Mn when the cycling life increased from the 3rd cycle to the 80th cycle, suggesting the formation of O vacancy. The change of

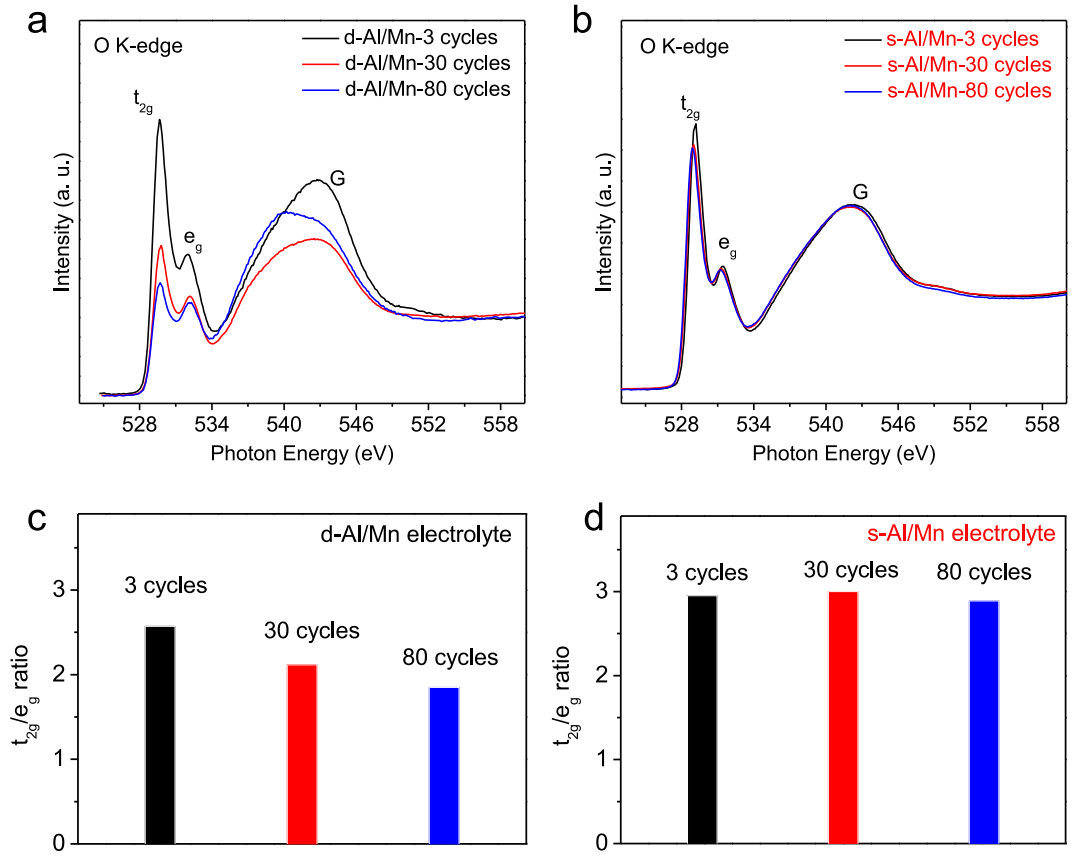

Fig. 5. O K-edge XAS of deposited MnO_2 after 3, 30 and 80 cycles in (a) d-Al/Mn and (b) s-Al/Mn electrolytes. t_{2g}/e_g ratios estimated from O K-edge spectra at various charge states in (c) d-Al/Mn and (d) s-Al/Mn electrolytes.

the broad post-edge features can be attributed to the distortion of the crystal structure. As shown in Fig. 5a, the broad G peak distorted with the increasing of cycling number, which implied that the intercalated Al^{3+} ions induce the change of the lattice structures. The distortion of MnO_2 lattice structure is unfavorable for the extraction of Al^{3+} ions. While in the electrolyte of s-Al/Mn, owing to the high reversibility of MnO_2 cathode, no visible change could be observed in the peaks of t_{2g}, e_g and G (Fig. 5b). In addition, t_{2g}/e_g ratios showed only a small change (Fig. 5d). The XAS results further illustrated that the solvation structures of Al^{3+} cations in the electrolyte of s-Al/Mn contribute to the high reversibility of the MnO_2/Mn^{2+} reactions by completely eliminating the Al^{3+} intercalation into MnO_2 lattice structure, thus achieving the highly stable Al/MnO_2 battery.

3. Conclusion

In conclusion, the solvation structures of Al^{3+} ions were tuned by concentrating electrolyte to form larger clusters of $AlCl_{1.8}(H_2O)_{4.2}{}^{1.2+}$ that are unavailable in the diluted electrolytes. The large radius of $AlCl_{1.8}(H_2O)_{4.2}{}^{1.2+}$ cations avoided self-intercalation into MnO_2 lattice and guaranteed the high reversibility of MnO_2 cathode in the MnO_2/Mn^{2+} deposition/stripping chemistry. In the optimized electrolyte, the newly developed Al/MnO_2 full cell delivered an enhanced battery performance with a high discharge plateau of ~1.9 V, a large specific capacity of ~493 mAh/g and long-term stability of over 1000 cycles. While in the diluted electrolyte, the performance decayed very fast (less than 130 cycles with two discharge plateaus positioned at 1.9 V and 1.6 V). Our molecular dynamic simulations and experimental results demonstrated that no Al^{3+} cations can be intercalated into MnO_2 by tuning their solvation structures in concentrated electrolyte, which was the key for the greatly improved performance of the Al/MnO_2 battery. This study opens new avenues to the development of Al batteries with high reversibility, which could be applied to other multivalent batteries.

4. Experimental section/methods

4.1. Materials

All reagents and materials in this work are commercially available and were used without further purification. Aluminum foil (Al, 99%), Aluminum chloride hexahydrate ($AlCl_3{\cdot}6H_2O$, ≥ 98.0%), manganese chloride tetrahydrate ($MnCl_2{\cdot}4H_2O$, ≥ 99.0%), hydrochloric acid (HCl, 95.0–98.0%) were purchased from Guoyao Corporation.

4.2. Al/MnO_2 cell assembly

The aqueous Al/MnO_2 battery was assembled using carbon felt (1.2×1.5 cm^2) as the cathode-less current collector and Al foil (1.2×1.5 cm^2) as the anode. Carbon felt was treated by plasma for 5 min and Al foil was polished by sandpaper before use. 1 M $MnCl_2$ + 1 M $AlCl_3$ in H_2O and 4.4 M $AlCl_3$ + 1 M $MnCl_2$ in H_2O with 0.05 M HCl were used as the electrolytes for Al/MnO_2 battery. The addition of HCl can help improve the redox reversibility of Mn^{2+}/MnO_2, which was well studied by previous work [18–20].

4.3. Characterization

Powder diffraction X-ray (PXRD) patterns were collected on a Philips X'Pert PRO SUPER Xray diffractometer equipped with graphite monochromatized Cu K_α radiation. Scanning electron microscope (SEM, JEOL-6700F) was carried out to characterize the morphologies, sizes

and structures of the MnO_2. Valence state measurements were characterized by X-ray photoelectron spectroscopy (XPS) using a monochromatic Al K_{a1} source (1486.6 eV). For the XRD, SEM and XPS measurements the carbon felt cathodes were washed with deionized water at least three times to avoid residuals and dried overnight in a vacuum oven before tests. O K-edge XAS test was carried out at the Catalysis and Surface Science Endstation at the BL11U beamline in the National Synchrotron Radiation Laboratory (NSRL) in Hefei, China.

4.4. Electrochemical tests

The cycling performance and rate capability of the cells were tested on a battery testing system (Landt, Wuhan, China). In the charge-discharge measurements, a technique of constant current with 1.4 V cut-off potential was used for the discharge process and a constant potential 2.2 V with cut-off capacity was applied to the charge process of the cells. The cyclic voltammetry and the electrochemical impedance spectra with a frequency range of 100 kHz to 1 Hz were collected using a Biologic electrochemical work station (Biologic, France). All electrochemical tests were conducted at room temperature.

4.5. Simulation details

All MD simulations in this work were performed in NVT ensemble using LAMMPS package [33]. The temperature of electrolyte was maintained at 300 K by the Nosé-Hoover thermostat with an integration time step of 1 fs [34]. 3D periodic boundary condition was applied. A combination of electrostatic and Lennard-Jones (LJ) potential was employed to describe the nonbonding interactions. SPC/E water model was used [35] and LJ potential of ions Al^{3+}, Mn^{2+} and Cl^- were from ref. [36–38]. The geometric mixing rule was applied to generate the Lennard-Jones parameters between different atom pairs. The cut-off of LJ potential and the real space electrostatic interaction are 10 Å. The long-range electrostatic interaction was solved by particle-particle particle-mesh (PPPM) algorithm [39]. The C–H bond was maintained by the SHAKE algorithm [40]. The MD simulation of both electrolyte systems were first heated up from 1 K to 300 K in 3 ns in NVT ensemble. Then the systems were equilibrated at 300 K for 2 ns in NVT ensemble and for 5 ns in NPT ensemble. At last, a 10-ns production run was used for data analysis.

Declaration of Competing Interest

The authors declare that they have no known competing financial interests or personal relationships that could have appeared to influence the work reported in this paper.

CRediT authorship contribution statement

Yan Xu: Conceptualization, Methodology, Writing – original draft. **Jiale Ma:** Formal analysis. **Taoli Jiang:** Formal analysis. **Honghe Ding:** Investigation. **Weiping Wang:** Formal analysis. **Mingming Wang:** Investigation. **Xinhua Zheng:** Investigation. **Jifei Sun:** Investigation. **Yuan Yuan:** Investigation. **Mingyan Chuai:** Investigation. **Na Chen:** Investigation. **Zhenyu Li:** Conceptualization, Methodology, Writing – review & editing. **Hanlin Hu:** Conceptualization, Methodology, Writing – review & editing. **Wei Chen:** Conceptualization, Methodology, Writing – review & editing, Project administration.

Acknowledgments

The work was supported by the startup funds from USTC (Grant # KY2060000150), China Postdoctoral Science Foundation (2021M693061), and National Natural Science Foundation of China (21825302). We acknowledge the support from USTC Center for Micro and Nanoscale Research and Fabrication, and Catalysis and Surface Science Endstation at the BL11U beamline in the National Synchrotron Radiation Laboratory (NSRL) in Hefei, China. This work was also supported by the Supercomputing Center of the USTC.

Supplementary materials

Supplementary material associated with this article can be found, in the online version, at doi:10.1016/j.ensm.2022.01.060.

References

[1] X.-.P. Gao, H.-.X. Yang, Multi-electron reaction materials for high energy density batteries, Energy Environ. Sci. 3 (2010) 174–189.
[2] C.-.X. Zu, H. Li, Thermodynamic analysis on energy densities of batteries, Energy Environ. Sci. 4 (2011) 2614–2624.
[3] V. Balland, M. Mateos, K. Harris, B. Limoges, The role of Al^{3+}-based aqueous electrolytes in the charge storage mechanism of MnO_x cathodes, Small 17 (2020) 2101515.
[4] J. Zheng, D.C. Bock, T. Tang, Q. Zhao, J. Yin, K.R. Tallman, G. Wheeler, X. Liu, Y. Deng, S. Jin, A.C. Marschilok, E.S. Takeuchi, K.J. Takeuchi, L.A. Archer, Regulating electrodeposition morphology in high-capacity aluminium and zinc battery anodes using interfacial metal–substrate bonding, Nat. Energy 6 (2021) 398–406.
[5] G.A. Elia, K. Marquardt, K. Hoeppner, S. Fantini, R. Lin, E. Knipping, W. Peters, J.-.F. Drillet, S. Passerini, R. Hahn, An overview and future perspectives of aluminum batteries, Adv. Mater. 28 (2016) 7564–7579.
[6] G.A. Elia, K.V. Kravchyk, M.V. Kovalenko, J. Chacón, A. Holland, R.G.A. Wills, An overview and prospective on Al and Al-ion battery technologies, J. Power Source. 481 (2021) 228870.
[7] J. Tu, W.-.L. Song, H. Lei, Z. Yu, L.-.L. Chen, M. Wang, S. Jiao, Nonaqueous rechargeable aluminum batteries: progresses, challenges, and perspectives, Chem. Rev. 121 (2021) 4903–4961.
[8] M.-.C. Lin, M. Gong, B. Lu, Y. Wu, D.-.Y. Wang, M. Guan, M. Angell, C. Chen, J. Yang, B.-.J. Hwang, H. Dai, An ultrafast rechargeable aluminium-ion battery, Nature 520 (2015) 324–328.
[9] H. Chen, F. Guo, Y. Liu, T. Huang, B. Zheng, N. Ananth, Z. Xu, W. Gao, C. Gao, A defect-free principle for advanced graphene cathode of aluminum-ion battery, Adv. Mater. 29 (2017) 1605958.
[10] S. Gu, H. Wang, C. Wu, Y. Bai, H. Li, F. Wu, Confirming reversible Al^{3+} storage mechanism through intercalation of Al^{3+} into V_2O_5 nanowires in a rechargeable aluminum battery, Energy Storage Mater. 6 (2017) 9–17.
[11] T. Mori, Y. Orikasa, K. Nakanishi, C. Kezheng, M. Hattori, T. Ohta, Y. Uchimoto, Discharge/charge reaction mechanisms of FeS_2 cathode material for aluminum rechargeable batteries at 55 °C, J. Power Source. 313 (2016) 9–14.
[12] T. Gao, X. Li, X. Wang, J. Hu, F. Han, X. Fan, L. Suo, A.J. Pearse, S.B. Lee, G.W. Rubloff, K.J. Gaskell, M. Noked, C. Wang, A rechargeable Al/S battery with an ionic-liquid electrolyte, Angew. Chem. Inter. Ed. 55 (2016) 9898–9901.
[13] L.D. Reed, E. Menke, The roles of V_2O_5 and stainless steel in rechargeable Al–ion batteries, J. Electrochem. Soc. 160 (2013) A915–A917.
[14] S. Liu, G.L. Pan, G.R. Li, X.P. Gao, Copper hexacyanoferrate nanoparticles as cathode material for aqueous Al-ion batteries, J. Mater. Chem. A 3 (2015) 959–962.
[15] C. Wu, S. Gu, Q. Zhang, Y. Bai, M. Li, Y. Yuan, H. Wang, X. Liu, Y. Yuan, N. Zhu, F. Wu, H. Li, L. Gu, J. Lu, Electrochemically activated spinel manganese oxide for rechargeable aqueous aluminum battery, Nat. Commun. 10 (2019) 73.
[16] Q. Zhao, M.J. Zachman, W.I. Al Sadat, J. Zheng, L.F. Kourkoutis, L. Archer, Solid electrolyte interphases for high-energy aqueous aluminum electrochemical cells, Sci. Adv. 4 (2018) eaau8131.
[17] S. He, J. Wang, X. Zhang, J. Chen, Z. Wang, T. Yang, Z. Liu, Y. Liang, B. Wang, S. Liu, L. Zhang, J. Huang, J. Huang, L.A. O'Dell, H. Yu, A high-energy aqueous aluminum-manganese battery, Adv. Funct. Mater 29 (2019) 1905228.
[18] H. Pan, Y. Shao, P. Yan, Y. Cheng, K.S. Han, Z. Nie, C. Wang, J. Yang, X. Li, P. Bhattacharya, K.T. Mueller, J. Liu, Reversible aqueous zinc/manganese oxide energy storage from conversion reactions, Nat. Energy 1 (2016) 16039.
[19] M. Chamoun, W.R. Brant, C.-.W. Tai, G. Karlsson, D. Noréus, Rechargeability of aqueous sulfate Zn/MnO_2 batteries enhanced by accessible Mn^{2+} ions, Energy Storage Mater. 15 (2018) 351–360.
[20] C. Yan, C. Lv, L. Wang, W. Cui, L. Zhang, K.N. Dinh, H. Tan, C. Wu, T. Wu, Y. Ren, J. Chen, Z. Liu, M. Srinivasan, X. Rui, Q. Yan, G. Yu, Architecting a stable high-energy aqueous Al-ion battery, J. Am. Chem. Soc. 142 (2020) 15295–15304.
[21] W. Pan, J. Mao, Y. Wang, X. Zhao, K.W. Leong, S. Luo, Y. Chen, D.Y.C. Leung, High--performance MnO_2/Al battery with in situ electrochemically reformed Al_xMnO_2 nanosphere cathode, Small Method. 9 (2021) 2100491.
[22] W. Chen, G. Li, A. Pei, Y. Li, L. Liao, H. Wang, J. Wan, Z. Liang, G. Chen, H. Zhang, J. Wang, Y. Cui, A manganese–hydrogen battery with potential for grid-scale energy storage, Nat. Energy 3 (2018) 428–435.
[23] D. Chao, W. Zhou, C. Ye, Q. Zhang, Y. Chen, L. Gu, K. Davey, S.-.Z. Qiao, An electrolytic Zn–MnO_2 battery for high-voltage and scalable energy storage, Angew. Chem. Inter. Ed. 58 (2019) 7823–7828.
[24] M. Wang, X. Zheng, X. Zhang, D. Chao, S.-.Z. Qiao, H.N. Alshareef, Y. Cui, W. Chen, Opportunities of aqueous manganese-based batteries with deposition and stripping chemistry, Adv. Energy Mater. 11 (2021) 2002904.
[25] G. Liang, F. Mo, H. Li, Z. Tang, Z. Liu, D. Wang, Q. Yang, L. Ma, C. Zhi, A universal principle to design reversible aqueous batteries based on deposition–dissolution mechanism, Adv. Energy Mater. 9 (2019) 1901838.
[26] J. Huang, L. Yan, D. Bin, X. Dong, Y. Wang, Y. Xia, An aqueous manganese–lead battery for large-scale energy storage, J. Mater. Chem. A 8 (2020) 5959–5967.

[27] L. Qian, W. Yao, R. Yao, Y. Sui, H. Zhu, F. Wang, J. Zhao, C. Zhi, C. Yang, Cations coordination-regulated reversibility enhancement for aqueous Zn-ion battery, Adv. Funct. Mater. 40 (2021) 2105736.
[28] J. Hu, H. Guo, Y. Li, H. Wang, Z. Wang, W. Huang, L. Yang, H. Chen, Y. Lin, F. Pan, Understanding Li-ion thermodynamic and kinetic behaviors in concentrated electrolyte for the development of aqueous lithium-ion batteries, Nano Energy 89 (2021) 106413.
[29] H. Berendsen, J.R. Grigera, T. Straatsma, The missing term in effective pair potentials, J. Phys. Chem. 91 (1987) 6269–6271.
[30] F. Wang, O. Borodin, T. Gao, X. Fan, W. Sun, F. Han, A. Faraone, J.A. Dura, K. Xu, C. Wang, Highly reversible zinc metal anode for aqueous batteries, Nat. Mater 17 (2018) 543–549.
[31] L. Suo, O. Borodin, T. Gao, M. Olguin, J. Ho, X. Fan, C. Luo, C. Wang, K. Xu, Water-in-salt" electrolyte enables high-voltage aqueous lithium-ion chemistries, Science 350 (2015) 938–943.
[32] R.K. Guduru, J.C. Icaza, A brief review on multivalent intercalation batteries with aqueous electrolytes, Nanomaterials 6 (2016) 41.
[33] S. Plimpton, Fast parallel algorithms for short-range molecular dynamics, J. Comput. Phys. 117 (1995) 1–19.
[34] W.G. Hoover, Canonical dynamics: equilibrium phase-space distributions, Phys. Rev. A 31 (1985) 1695–1697.
[35] L.X. Dang, Mechanism and thermodynamics of ion selectivity in aqueous solutions of 18-crown-6 ether : a molecular dynamics study, J. Am. Chem. Soc. 117 (1995) 6954–6960.
[36] P. Li, B.P. Roberts, D.K. Chakravorty, K.M. Merz, Rational design of particle Mesh Ewald compatible Lennard-Jones parameters for +2 metal cations in explicit solvent, J. Chem. Theory Comput. 9 (2013) 2733–2748.
[37] P. Li, L.F. Song, K.M. Merz, Systematic parameterization of monovalent ions employing the nonbonded model, J. Chem. Theory Comput. 11 (2015) 1645–1657.
[38] P. Li, L.F. Song, K.M. Merz, Parameterization of highly charged metal ions using the 12-6-4 LJ-type nonbonded model in explicit water, J. Phys. Chem. B 119 (2015) 883–895.
[39] R.W. Hockney, J.W. Eastwood, Computer Simulation Using Particles, CRC Press, 1988.
[40] H.C. Rattle Andersen, A "Velocity" version of the shake algorithm for molecular dynamics calculations, J. Comput. Phys. 52 (1983) 24–34.